Asymmetric transition of electrical resistance in an all-solid-state redox device with Fe_3O_4 and Li-ion electrolyte thin films for physical reservoir computing

Wataru Namiki[1], Takashi Tsuchiya[1]*, Daiki Nishioka[1,2], Tohru Higuchi[2], and Kazuya Terabe[1]

[1]*National Institute for Materials Science, Tsukuba, Ibaraki 305-0044, Japan*

[2]*Tokyo University of Science, Katsushika, Tokyo 125-8585, Japan*

E-mail: TSUCHIYA.Takashi@nims.go.jp

In recent years, ion-gating devices have been used in artificial neuromorphic computing and achieved high performance for time-series data processing. However, the origin of such performance still needs to be clarified. In this study, we fabricated an all-solid-state redox device with functional material Fe_3O_4 and Li-ion conducting solid electrolytes, and the transient response of the electrical resistance of the Fe_3O_4 thin film to time-series data input was investigated. The transition between high and low electrical resistance states was asymmetry, and residual Li-ion in the thin film led to a hysteresis effect. These unique features, which is induced by ion-electron dynamics coupling, contributes to the high performance of physical reservoir computing utilizing ion-gating device.

1. Introduction

There is a strong demand to develop artificial intelligence devices to process information that increases explosively and efficiently. Several studies have been recently conducted to realize artificial neural network systems that can process various information on terminal devices using physical devices.[1-7] Recently, reservoir computing, which can process time series data with a small learning cost, has been attracting attention, and attempts to process time series data with high accuracy using nonlinear responses and short-term memory of physical devices have been vigorously pursued.[8-26] Among these, an all-solid-state ion-gating device, which is one of the ionic devices,[27-36] can control the physical properties (not only electrical properties but also magnetic and optical properties) of functional materials by transporting ions,[37-53] and the modulated electrical properties can be used in artificial neural networks and artificial retina.[54-59] It has been demonstrated that ion-gating performs highly in image recognition and time series data prediction tasks.[22-24] However, the origin of the high performance needs to be clarified, and the details of the internal state change of the functional material in response to time series data input, which is converted to voltage, need to be investigated. In ion-gating, electronic carriers are injected into the functional material via charge compensation along with the transport of ions.[33-35,37-43,45-53] Therefore, measuring electrical resistance is a powerful probe method to understand the internal state of functional materials. Herein, we fabricated an all-solid-state reduction/oxidation (redox) device by stacking a functional material and a solid electrolyte and focused on the transient response of the electrical resistance of the functional materials to time-series data input duration to clarify changes in the internal state (i.e., electrical resistance) of the functional materials.

In this study, we adopted Fe_3O_4, which is known to operate as an artificial neural network device as well as to control the electrical and magnetic properties (magnetization and magnetization direction) of Fe_3O_4 to a large extent by voltage when combined with a solid electrolyte, for a functional material.[43,48,60-62] Lithium-ions in the solid electrolyte diffuse into the lattice of Fe_3O_4 by applying voltage, and such inserted ions modulate a number of electronic carriers ($>10^{21}$ cm^{-3}) in Fe_3O_4 thin film.[43,48, 63] Since Li-ions are driven by the electric field that depends on the series resistance of the Fe_3O_4 thin film and the solid electrolyte, it was found that by inputting time series data consisting of random voltages, the effective electric field to Li-ion is modulated by the electrical resistance of Fe_3O_4 that

changes sequentially and shows various transient responses.

2. Experimental methods

A 12-nm-thick magnetite thin film was deposited on a flat surface of a MgO (110) substrate by pulsed laser deposition (PLD) using a magnetite polycrystalline target. The area of the thin film was 500 × 700 μm^2. The base pressure in the deposition chamber was 3.3 × 10^{-5} Pa. The substrate temperature was kept at 573 K, A flow rate of the Ar (99 %) and O_2 (1%) mixture gas was fixed at 0.2 sccm, and the pressure was kept at 1.3 × 10^{-3} Pa during deposition.[48] A 5-nm-thick Ti adhesion layer and 50-nm-thick Pt electrode with a Hall-bar shape were continuously deposited on the magnetite thin film by rf magnetron sputtering. Then, A Li_2O-SiO_2-ZrO_2 (LSZO) thin film was deposited by PLD, using a Li-excess LSZO ceramic target, in a 3.4 Pa O_2 atmosphere at a flow rate of 8.5 sccm. Finally, the Au gate electrode was deposited on the LSZO electrolyte by rf magnetron sputtering. Metal shadow masks were used to pattern each layer.

A micro-Raman spectroscope, which has incident light with a wavelength of 573 nm and a power of 0.5 mW to avoid thermal oxidation, was used to evaluate the quality of the magnetite thin film. The exposure times and accumulation were set to 120 seconds and 20 times.

Electrical measurement was performed on the device in a high vacuum chamber (< 10^{-3} Pa) using a Keithley 4200-SCS parameter analyzer. Five pulse trains with different pulse periods (50, 75, 100, 150, and 200 seconds) were prepared to investigate responses to various inputs. Each pulse train had a base voltage of 1.0 V and an amplitude range of [0.5, 1.5 V]. Five pulse trains were input one by one with time intervals in between. Drain current I_D was set to 3 μA during the measurement, and voltage drop V_{XX} was acquired as information on electrical resistance modulated by ion-gating. The following equation was used to calculate the relaxation time τ.[57]

$$V_{XX} = Aexp\left[-\left(\frac{t-t_0}{\tau}\right)\right] + V_\infty \quad (1).$$

where A, t, t_0, and V_∞ denote the amplitude of V_{XX} response, retention time, the pulse-on finished time, and the base level of V_{XX} at the corresponding pulse-on period.

3. Results and discussion

3.1 Results

Figure 1(a) shows a schematic illustration of a fabricated device consisting of a magnetite channel, electrodes for electrical measurement, LSZO electrolyte film, and gate electrodes. Raman peaks, which are located at 669 cm^{-1}, 542 cm^{-1}, and 310 cm^{-1}, of the magnetite thin film were assigned by A_{1g}, $T_{2g}(2)$, and $T_{2g}(3)$, and there is no impurity (e.g., FeO, Fe_2O_3, and so on), as shown in Fig. 1(b).[43,48] Figure 1(c) shows a transmission electron microscope (TEM) image of cross-section of a fabricated device and its fast Fourier transformation (FFT). It was successfully confirmed that the thin film was grown epitaxially on the surface of MgO (110) substrate.[48]

The electrical property of said device was evaluated by measuring drain current I_D, which was modulated by gate voltage V_G sweeping, as shown in Fig. 2(a). I_D flowing in the channel thin film was enhanced as V_G increased from 0.0 V to 2.0 V, resulting from electronic carrier doping induced by Li-ion migrating to the Fe_3O_4 side. On the other hand, I_D was reduced as V_G decreased from 1.0 V to 0.0 V, resulting from removing the electronic carrier induced by Li-ion migrating to the gate electrode side. On this I_D modulation, large hysteresis was observed due to relatively slow migration in the Fe_3O_4, indicating that Li-ion was inserted in and deserted from Fe_3O_4. Here, magnetite has 24 Fe ions, which are 8 tetrahedral Fe ions (Fe_{8a}) and 16 octahedral Fe ions (Fe_{16d}), and 32 O ions (O_{32e}) in a unit cell. Li-ion inserted in the magnetite is located at the 16c site, which has an octahedral vacant center surrounded by 6 oxygen ions, as shown in Fig. 2(b).[64] While Fe_{8a} ion is trivalent and has five down-spins in d orbit, Fe_{16d} ion has a mixed valence state due to the co-existence of trivalent and divalent Fe ions, and trivalent Fe ion has five up-spins and divalent Fe ion has a down-spin in addition to five up-spins. Down spin at Fe_{16d} contributes to electrical conduction.[65] Thus, when the I_D was enhanced (reduced), electron was doped (removed) in trivalent (divalent) Fe_{16d} through reduction (oxidation), increasing the number of down-spin of Fe_{16d}.[43] Such electronic carrier tuning induced by insertion and desertion of Li-ion showed large hysteresis with slow relaxation. This hysteresis effect indicates that the present state has information based on the past state induced by input at the past step.[23,24] We will examine how this hysteresis affects the dynamics of ions and electrons during input of the random wave used in the time-series data processing task.

Figure 3(a) shows a measurement configuration of V_{XX} response in proportion to electrical resistance for time-series data inputs. A time-series voltage has a pulsed shape with 50 steps and is input as V_G. I_D was fixed at 3 μA, and potential drop V_{XX} was acquired during the V_G inputs. The horizontal axis of the V_{XX} signal was normalized to compare the shape of the signals measured at various pulse periods. Figure 3(b) shows the V_{XX} response for the V_G input in a cropped region of normalized time, corresponding to a time step k, ranging from 559 to 579. Here, k is a pulse period with pulse-on and pulse-off. As the pulse period of V_G was extended, the degree of modulation in V_{XX} became larger since the amount of doped electronic carrier was increased during its application time. Then, V_{XX} decreased while maintaining said trend in the pulsed-off interval. In addition to such modulation rate variation at various pulse periods, we evaluated the relaxation time of V_{XX} response under pulse voltage application. Figures. 3(c) and 3(d) show relaxation time variations in pulse-on and pulse-off durations at various k. Although relaxation time in pulse-on duration was longer than that in pulse-off duration (asymmetric transient response of V_{XX} at each k) in the entire range, the relaxation times of both durations increased as the pulse period extended. Furthermore, relaxation time variation resulted from the input of time-series voltage, and it was found that the relaxation time of electronic carrier tuning, induced by ion and electron migrations, positively correlates with the amplitude of voltage input. Thus, an ion-gating device shows a non-single transient response with various relaxation times by the input with various intensities, and a variety of outputs can be obtained by inputting the time-series voltage.

Fig. 4(a) shows the V_{XX} response for input pulse voltages train in a cropped region of normalized time ranging from 750 (time step of k_{39}) to 850 (time step of k_{42}) to investigate a detail of relaxation time, which depends on input amplitude. The difference is that the amount of change in V_{XX} was more significant as the pulse period became longer and resulted from the more considerable amount of tuned electronic carrier density due to the longer application time of V_G. V_{XX} amplitude variation at each k was not in good agreement with input amplitude variation, shown as red and blue dashed lines described in the figures for pulse-on and pulse-off. This inconsistency results from said asymmetric transition response, induced by ion-gating, of the electrical resistance state. Those relaxation times in pulse-on and pulse-off durations are plotted in the upper and lower panels of Fig. 4(b). The extension

of the pulse period not only lengthened the relaxation time but also changed the shape of the k-dependence of the relaxation time as follows. For a pulse-on time, the variation of relaxation time was slight for short pulse periods of 100 seconds or less, but the variation of relaxation time increased for more extended pulse periods of 150 seconds or more, as shown in an upper panel of Fig. 4(b). Then, the relaxation time of k_{39} was considerably expanded, and the variation of relaxation time after k_{40} became small, as shown in the upper panel of Fig. 4(c).

On the other hand, the change in the distribution of relaxation times for pulse-off duration was different from that of the pulsed-on one, as shown in a lower panel of Fig. 4(b). While up-turn convexity was shown below shorter intervals of 75 seconds, down-turn convexity was shown above longer intervals of 150 seconds via approximate flat distribution at the interval of 100 seconds. This is because the increase in relaxation time at k_{40} was smaller than those at other ks, as shown in a lower panel of Fig. 4(c). From these results, dynamics driven by voltage application in ion-gating devices showed the asymmetric transition between high V_{XX} and low V_{XX} states.

3.2 Discussion

Here, we discuss the origins of asymmetric transition between high V_{XX} and low V_{XX} states. Figure 4(d) shows schematic illustrations of transitions between the low electrical resistance (R) state and the high R state of the channel of the ion-gating device. Ion-gating leads to R modulation of the Fe_3O_4 thin film through redox reaction. The Fe_3O_4 thin film possesses a large amount of Li-ions in its lattice in a low R state, and those Li-ions are removed from the lattice by V_G application.[43,48] The Li-ion was driven by an electric field, and the electric field depends on R of the thin film (R_C) and R of the solid electrolyte (R_{SE}). This is because the electrical equivalent circuit between the gate and source electrodes is described as a series circuit of R_C and R_{SE}. Here, the total R (R_{total}) can be described as follows:

$$R_{\mathrm{total}} = R_{\mathrm{C}} + R_{\mathrm{SE}}, \qquad (2)$$

Moreover, voltage potential between gate and source electrodes (i.e., V_G) is expressed using eq. (2) as shown below,

$$V_{\mathrm{G}} = I_{\mathrm{G}} R_{\mathrm{total}} = I_{\mathrm{G}}(R_{\mathrm{C}} + R_{\mathrm{SE}}). \qquad (3)$$

Then, eq. (3) can be transformed as follows.

$$I_{\mathrm{G}} = \frac{dQ}{dt} = \frac{V_{\mathrm{G}}}{(R_{\mathrm{C}}+R_{\mathrm{SE}})}, \qquad (4)$$

where I_{G} and Q denote electrical current flowing in the equivalent circuit, and the amount of electrical charge, which corresponds to Li-ion of the solid electrolyte and electronic carrier modulated by redox reaction, and dQ/dt shows the amount of flowing Q per a unit of time t. When R_{C} is reduced by V_{G} application, I_{G} and dQ/dt become large since V_{G} and R_{SE} are constants. In short, the effective electric field affecting Li-ion varied with the R_{C} state and said the electric field was large (small) when R_{C} was low (high) by Li-ion insertion (desertion) due to a slight potential drop in the Fe_3O_4 and a significant potential drop in the solid electrolyte. This variation in the electric field leads to variation in the transition speed of the R_{C} state, meaning that the transition from low R_{C} to high R_{C} is faster, and the transition from high R_{C} to low R_{C} is slower. This is the origin of asymmetric transition response of V_{XX}. Furthermore, some of the inserted Li-ions remained in the thin film, resulting in the inconsistency between V_{XX} amplitude and input amplitude in Fig. 4(a). These ions contribute to the hysteresis effect observed in the V_{XX} response for time-series V_{G} input. This study found that ion-gating leads to electronic carrier density modulation accompanied by unique features, such as asymmetric transition and hysteresis effect. These are critical features for implementing physical reservoir computing, which requires nonlinearity (asymmetric transition response) and short-term memory (hysteresis effect).[22-24)]

4. Conclusions

We fabricated an all-solid-state redox device with Fe_3O_4 and Li-ion electrolyte thin films and measured the V_{XX} response of the said device under a random V_{G} train input to investigate the origin of a performance as an artificial neuromorphic device through the internal state (i.e., electrical resistance) of the Fe_3O_4 thin film. It was found that the transition of *the R* state was asymmetric, and the information of V_{G} input at the past step remained as residual Li-ions in the thin film. This asymmetric behavior and hysteresis can satisfy essential requirements (i.e., nonlinearity and short-term memory) for reservoir computing. This study indicates that the asymmetry and hysteresis contribute to such performance. Furthermore, the performance can be improved by modulation of these features appearing in the device through material engineering to optimize its response speed.[66)]

Acknowledgments

This work was supported in part by the Japan Society for the Promotion of Science (JSPS) KAKENHI Grant numbers, JP22H04625 (Grant-in-Aid for Scientific Research on Innovative Areas “Interface Ionics”) and JP22KJ2799 (Grant-in-Aid for JSPS Fellows), and JST PRESTO (Grant number, JPMJGX23S2). Part of this work was supported by the Iketani Science and Technology Foundation and JFE 21st century foundation. Part of this work was supported by the Electron microcopy unit of the National Institute for Materials Science.

References

1) T. Ohno, T. Hasegawa, T. Tsuruoka, K. Terabe, J. K. Gimzewski, and M. Aono, Nat. Mater. **10**, 591 (2011).
2) H. O. Sillin, R. Aguilera, H. -H. Shieh, A. V. Avizienis, M. Aono, A. Z. Stieg, and J. K. Gimzewski, Nanotechnology **24**, 384004 (2013).
3) R. Nur, T. Tsuchiya, K. Toprasertpong, K. Terabe, S. Takagi, and M. Takenaka, Nanoscale **14**, 2013 (2022).
4) H.-M. Huang, Z. Wang, T. Wang, Y. Xiao, and X. Guo, Adv. Intell. Syst. **2**, 2000149 (2020).
5) A. M. Hammond and R. M. Camacho, Opt. Exp. **27**, 29620 (2019).
6) S. Jung, H. Lee, S. Myung, H. Kim, S. K. Yoon, S.-W. Kwon, Y. Ju, M. Kim, W. Yi, S. Han, B. Kwon, B. Seo, K. Lee, G.-H. Koh, K. Lee, Y. Song, C. Choi, D. Ham and S. J. Kim, Nature **601**, 211 (2020).
7) J. M. Goodwill, N. Prasad, B. D. Hoskins, M. W. Daniels, A. Madhavan, L. Wan, T. S. Santos, M. Tran, J. A. Katine, P. M. Braganca, M. D. Stiles, and J. J. McClelland, Phys. Rev. Appl. **18,** 014039 (2022).
8) H. Jaeger and H. Haas, Science **304**, 78 (2004).
9) W. Maass, T. Natschläger, and H. Markram, Neural Comput. **14**, 2531 (2002).
10) D. Verstraeten, B. Schrauwen, M. D'Haene, and D. Stroobandt, Neural Networks **20**, 391 (2007).
11) L. Appeltant, M. C. Sorano, G. van der Sande, J. Danckaert, S. Massar, J. Dambre, B. Schrauwen, C. R. Mirasso, and I. Fischer, Nat. Commun. **2**, 468 (2011).
12) C. Du, F. Cai, M. A. Zidan, W. Ma, S. H. Lee, and W. D. Lu, Nat. Commun. **8**. 2204 (2017).
13) S. Kan, K. Nakajima, T. Asai, and M. A. Kasaya, Adv. Sci. **9**, 2104076 (2022).
14) M. A. Kasaya, Y. Takeshima, S. Kan, K. Nakajima, T. Oya, and T. Asai, Neuromorph. Comput. and Eng. **2**, 014003 (2022).
15) J. Torrejon, M. Riou, F. A. Araujo, S. Tsunegi, G. Khalsa, D. Querlioa, P. Bortolotti, V. Cros, K Yakushiji, A. Fukushima, H. Kubota, S. Yuasa, M. D. Stiles, and J. Grollier, Nature **547**, 428 (2017).
16) R. Nakane, G. Tanaka, and A. Hirose, IEEE Access **6**, 4462 (2018).
17) R. Nakane, A. Hirose, and G. Tanaka, Phys. Rev. Res. **3**, 033243 (2021).
18) R. Nakane, A. Hirose, and G. Tanaka, Phys. Rev. Appl. **19**. 034047 (2023).

19) W. Namiki, D. Nishioka, Y. Yamaguchi, T. Tsuchiya, T. Higuchi, and K. Terabe, Adv. Intell. Syst. 2300238 (2023).
20) Q. Vinckier, F. Duport, A. Smerieri, K. Vandoorne, P. Bienstman, M. Haelterman, and S. Massar, Optica **2**, 438 (2015).
21) K. Nakajima, H. Hauser, T. Li, and R. Pfeifer, Sci. Rep. **5**, 10487 (2015).
22) D. Nishioka, T. Tsuchiya, W. Namiki, M. Takayanagi, M. Imura, Y. Koide, T. Higuchi, and K. Terabe, Sci. Adv. **8**, eade1156 (2022).
23) T. Wada, D. Nishioka, W. Namiki, T. Tsuchiya, T. Higuchi, and K. Terabe, Adv. Intell. Syst. **5**, 2300123 (2023).
24) K. Shibata, D. Nishioka, W. Namiki, T. Tsuchiya, T. Higuchi, and K. Terabe, Sci. Rep. **13**, 21060 (2023).
25) B. Brazani, G. Dion, J.-F. Morissette, L. Beaudoin, and J. Sylvestre, and J. Microelectromech. Sys. **29**, 338 (2020).
26) J. C. Gartside, G. D. Stenning, A. Vanstone, H. H. Holder, D. M. Arroo, T. Dion, F. Caravelli, H. Kurebayashi, and W. R. Branford, Nat. Nanotech. **17**, 460 (2022).
27) D. Y. Kim, S. Miyoshi, T. Tsuchiya, and S. Yamaguchi, ECS Trans. **45**, 161 (2012).
28) W. Namiki, M. Takayanagi, K. Horiba, M. Kobayashi, M. Minohara, H. Kumigashira, and T. Higuchi. ECS Trans. **75**, 83 (2017).
29) W. Namiki, T. Tsuchiya, M. Takayanagi, S. Furuichi, M. Minohara, M. Kobayashi, K. Horiba, H. Kumigashira, and T. Higuchi, J. Phys. Soc. Jpn. **86**, 074704 (2017).
30) W. Namiki, T. Tsuchiya, M. Takayanagi, K. Kawamura, T. Kawaguchi, and T. Higuchi, Trans. Mater. Res. Soc. Jpn. **43**, 175 (2018).
31) T. Tsuchiya, S. Miyoshi, Y. Yamashita, H. Yoshikawa, K. Terabe, K. Kobayashi, S. Yamaguchi, Solid State Ionics **253**, 110 (2013).
32) D. Nishioka, T. Tsuchiya, W. Namiki, M. Takayanagi, K. Kawamura, T. Fujita, R. Yukawa, K. Horiba, H. Kumigashira, and T. Higuchi, Nanoscale Res. Lett. **15**, 42 (2020).
33) K. Terabe, T. Tsuchiya, and T. Tsuruoka, Adv. Electron. Mater. **8**, 2100645 (2022).
34) T. Tsuchiya, K. Terane. R. Yang, and M. Aono, Jpn. J. Appl. Phys. **55**, 1102A4 (2016).
35) T. Tsuchiya, M. Imura, Y. Koide, and K. Terabe, Sci. Rep. **7**, 10534 (2017).
36) D. Kan, T. Hatano, A. Abe, H. Ikuta, and Y. Shimakawa, Appl. Phys. Lett. **117**, 231602 (2020).

37) T. Tsuchiya, K. Terabe, and M. Aono, Appl. Phys. Lett. **103**, 073110 (2013).
38) T. Tsuchiya, K. Terabe, and M. Aono, Adv. Mater. **26**, 1087 (2014).
39) T. Tsuchiya, K. Terabe, and M. Aono, Appl. Phys. Lett. **105**, 183101 (2014).
40) T. Tsuchiya, T. Tsuruoka, K. Terabe, and M. Aono, ACS Nano **9**, 2102 (2015).
41) T. Tsuchiya, M. Ochi, T. Higuchi, K. Terabe, and M. Aono, ACS Appl. Mater. Inter. **7** 12254 (2015).
42) T. Tsuchiya, S. Moriyama, K. Terabe, and M. Aono, Appl. Phys. Lett. **107**, 013104 (2015).
43) T. Tsuchiya, K. Terabe, M. Pchi, T. Higuchi, M. Osada, Y. Yamashita, S. Ueda, and M. Aono, ACS Nano **10**, 1655 (2016).
44) K. Terabe, T. Tsuchiya, R. Yang, and M. Aono, Nanoscale **8**, 13873 (2016).
45) T. Tsuchiya, M. Ochi, T. Higuchi, and K. Terabe, Jpn, J. Appl. Phys. **55**, 06GJ03 (2016).
46) T. Tsuchiya, T. Tsuruoka, S.-J. Kim, K. Terabe, and M. Aono, Sci. Adv. **4**, eaau2057 (2018).
47) D. Nishioka, T. Tsuchiya, T. Higuchi, and K. Terabe, Jpn. J. Appl. Phys. **59**, SIIG09 (2020).
48) W. Namiki, T. Tsuchiya, M. Takayanagi, T. Higuchi, and K. Terabe, ACS Nano, **14**, 16065 (2020).
49) T. Tsuchiya, M. Takayanagi, K. Mitsuishi, M. Imura, S. Ueda, Y. Koide, T. Higuchi, and K. Terabe, Commun. Chem. **4**, 117 (2021).
50) Y. Isoda, D. Kan, Y. Ogura, T. Majima, T. Tsuchiya, and Y. Shimakawa, Appl. Phys. Lett. **120**, 091601 (2022).
51) Y. Isoda, D. Kan, T. Majima, and Y. Shimakawa, Appl. Phys. Exp. **16**, 015506 (2023).
52) L. Xie, Y. Ishoda, T. Majima, Y. Shen, D. Kan, and Y. Shimakawa, J. Solid State Electrochem. https://doi.org/10.1007/s10008-023-05759-5
53) T. Wada, W. Namiki, T. Tsuchiya, D. Kan, Y. Shimakawa, T. Higuchi, and K. Terabe, Jpn. J. Appl. Phys. **61**, SM1002 (2022).
54) E. J. Fuller, F. E. Gabaly, F. Léonard, S. Agarwal, S. J. Plimpton, R. B. Jacobs-Gedrim, C. D. James, M. J. Marinella, and A. A. Talin, Adv. Mater. **29**, 1604310 (2017).
55) C. -S. Yang, D.-S. Shang, N. Liu, E. Fuller, S. Agrawal, A. A. Talin, Y.-Q. Li, B.-G. Shen, and Y. Sun, Adv. Funct. Mater. **28**, 1804170 (2018).
56) D. Nishioka, T. Tsuchiya, T. Higuchi, and K. Terabe, Neuromorph. Comput. and Eng. **3**, 034008 (2023).
57) M. Takayanagi, D. Nishioka, T. Tsuchiya, M. Imura, Y. Koide, T. Higuchi, and K. Terabe,

Mater. Today Adv. **18**, 100393 (2023).
58) H. N. Mohanty, T. Tsuruoka, J. R. Mohanty, and K. Terabe, ACS Appl. Mater. Interfaces **15**, 19279 (2023).
59) X. Wan, T. Tsuruoka, and K. Terabe, Nano Lett. **21**, 7938 (2021).
60) P. Monalisha, S. Li, S. G. Bhat, T. Jin, P. S. Ail Kumar, and S. N. Piramanayagam, J. Appl. Phys. **133**, 084901 (2023).
61) T. Miao, W. Liu, C. Huang, B. Cui, R. Chu, X. Zhao, X. Wu, S. Wu, J. Xie, H. Liu, J. Chen, B. Cheng, and G. Hu, J. Mater. Chem. C **11**, 7732 (2023).
62) V. P. Singh, C. P. Singh, H. Ranjan, and S. K. Pandey, Mater. Lett. **344**, 134431 (2023).
63) A. F. Pacheco, J. Orna, J. M. De Teresa, P. A. Algarabel, L. Morellon, J. A. Pardo, M. R. Ibarra, E. Kampert, U. Zeitler, Appl. Phys. Lett. **95**, 262108 (2009).
64) C. N. Lininger, C. A. Cama, K. J. Takeuchi, A. C. Marschilok, E. S. Takeuchi, A. C. West, M. S. Hybertsen, Chem. Mater. **30**, 7922 (2018).
65) A. Yanase and K. Siratori, J. Physic. Soc. Jpn. **53**, 312 (1984).
66) Xie, L., Isoda, Y., Majima, T. et al. Orientation-dependent electrochemical response of LaSrNiO4 epitaxial films. J Solid State Electrochem (2023). 10.1007/s10008-023-05759-5

Figure Captions

Fig. 1. (a) A schematic illustration of a fabricated all-solid-state redox device. LSZO denotes a Li_2O-SiO_2-ZrO_2 thin film. (b) A Raman spectrum of a Fe_3O_4 thin film deposited on MgO single crystal. (c) TEM image and its fast Fourier transform of a cross-section of the fabricated device shown in (a).

Fig. 2. (a) Normalized drain current I_D variation at various gate voltage V_G, measured with sweeping V_G. The sweeping rate is fixed at 0.9 mV/sec. (b) A part of a unit cell of Fe_3O_4 and spin configuration in 3d orbits of Fe_{8a} and Fe_{16d}. The red arrow denotes doped down spin with Li-ion (Li^+) insertion into the lattice.

Fig. 3. (a) A measurement configuration of an all-solid-state redox device to acquire voltage drop in Fe_3O_4 thin film V_{XX}. S and D denote source and drain electrodes. (b) V_{XX} response for a voltage pulse at a time step k, corresponding to a region colored gray surrounded by a dashed line. Relaxation time variations at various k in (c) pulse-on duration and (d) pulse-off duration.

Fig. 4. (a) V_{XX} response at the cropped region ranging from 750 (k_{39}) to 850 (k_{42}). Red (Blue) arrows denote V_{XX} amplitude and V_G amplitude in pulse-on (pulse-off) duration. (b) Relaxation time variation at the region ranging from k_{39} to k_{42}. (c) Pulse period dependence of relaxation time at various time steps. (d) Schematic principle of transition speed variation of redox reaction induced by pulse-on and pulse-off.

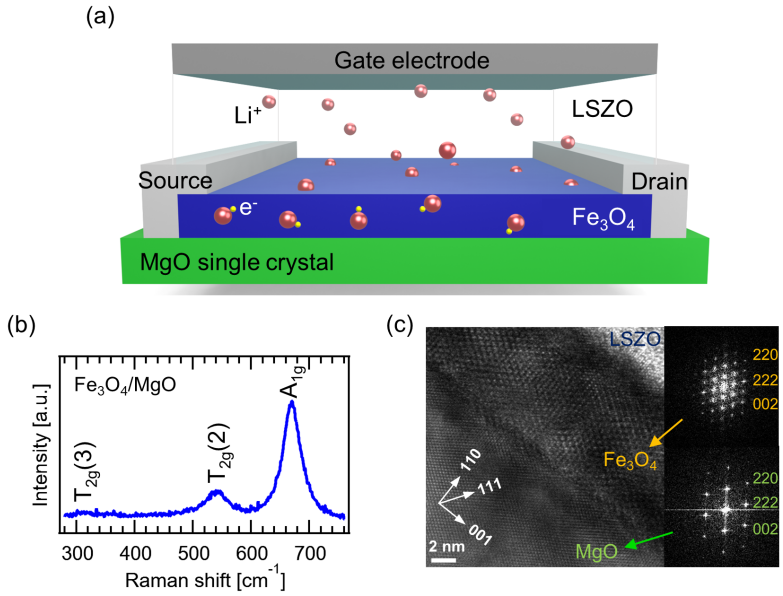
(a)
Gate electrode
Li+
LSZO
Source
Drain
e-
Fe3O4
MgO single crystal
(b)
Fe3O4/MgO
A1g
T2g(2)
T2g(3)
Intensity [a.u.]
300
400
500
600
700
Raman shift [cm-1]
(c)
LSZO
220
222
002
Fe3O4
110
111
001
220
222
002
2 nm
MgO

Fig.1.

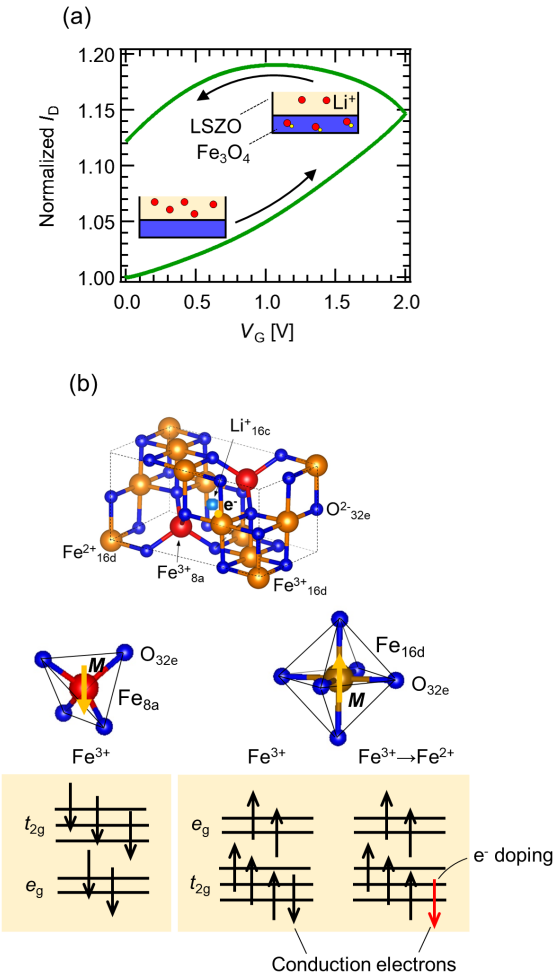
(a)
Normalized I_D
1.20
1.15
1.10
1.05
1.00
0.0
0.5
1.0
1.5
2.0
V_G [V]
LSZO
Fe_3O_4
Li^+
(b)
Li^+_{16c}
e^-
O^{2-}_{32e}
Fe^{2+}_{16d}
Fe^{3+}_{8a}
Fe^{3+}_{16d}
M
O_{32e}
Fe_{8a}
Fe^{3+}
Fe_{16d}
O_{32e}
M
Fe^{3+}
$Fe^{3+}\rightarrow Fe^{2+}$
t_{2g}
e_g
e_g
t_{2g}
e^- doping
Conduction electrons

Fig. 2.

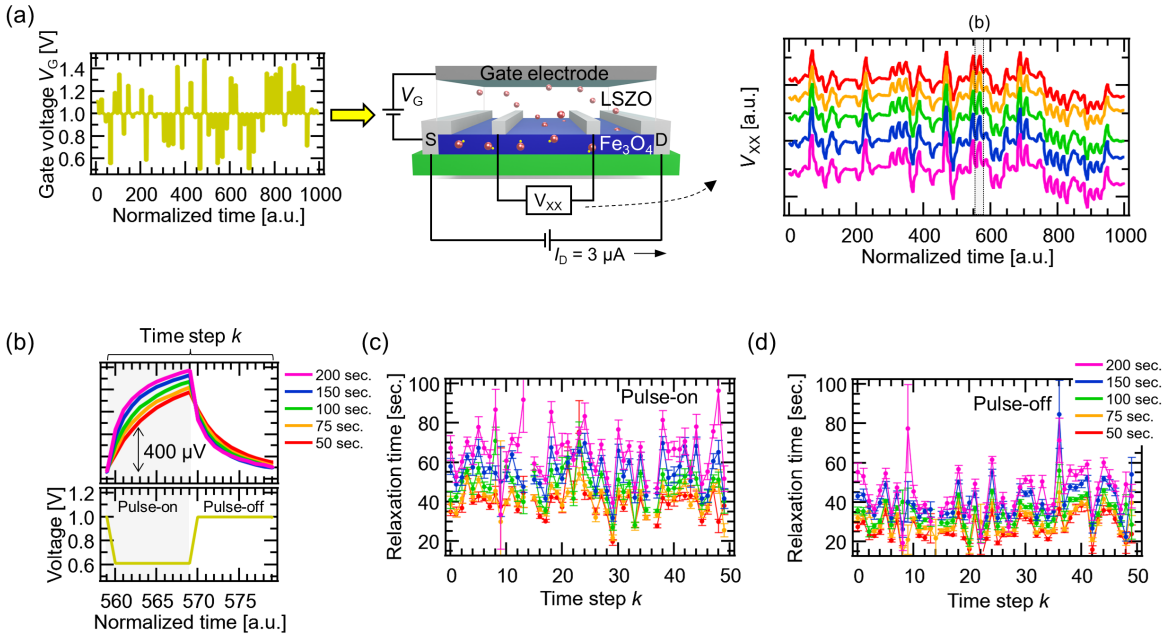
(a)
Gate voltage V_G [V]
1.4
1.2
1.0
0.8
0.6
0 200 400 600 800 1000
Normalized time [a.u.]
Gate electrode
V_G
LSZO
S
Fe_3O_4
D
V_{XX}
I_D = 3 μA
(b)
V_{XX} [a.u.]
0 200 400 600 800 1000
Normalized time [a.u.]
(b)
Time step k
400 μV
200 sec.
150 sec.
100 sec.
75 sec.
50 sec.
Pulse-on
Pulse-off
Voltage [V]
1.2
1.0
0.8
0.6
560 565 570 575
Normalized time [a.u.]
(c)
Relaxation time [sec.]
100
80
60
40
20
Pulse-on
0 10 20 30 40 50
Time step k
(d)
Relaxation time [sec.]
Pulse-off
200 sec.
150 sec.
100 sec.
75 sec.
50 sec.
0 10 20 30 40 50
Time step k

Fig. 3

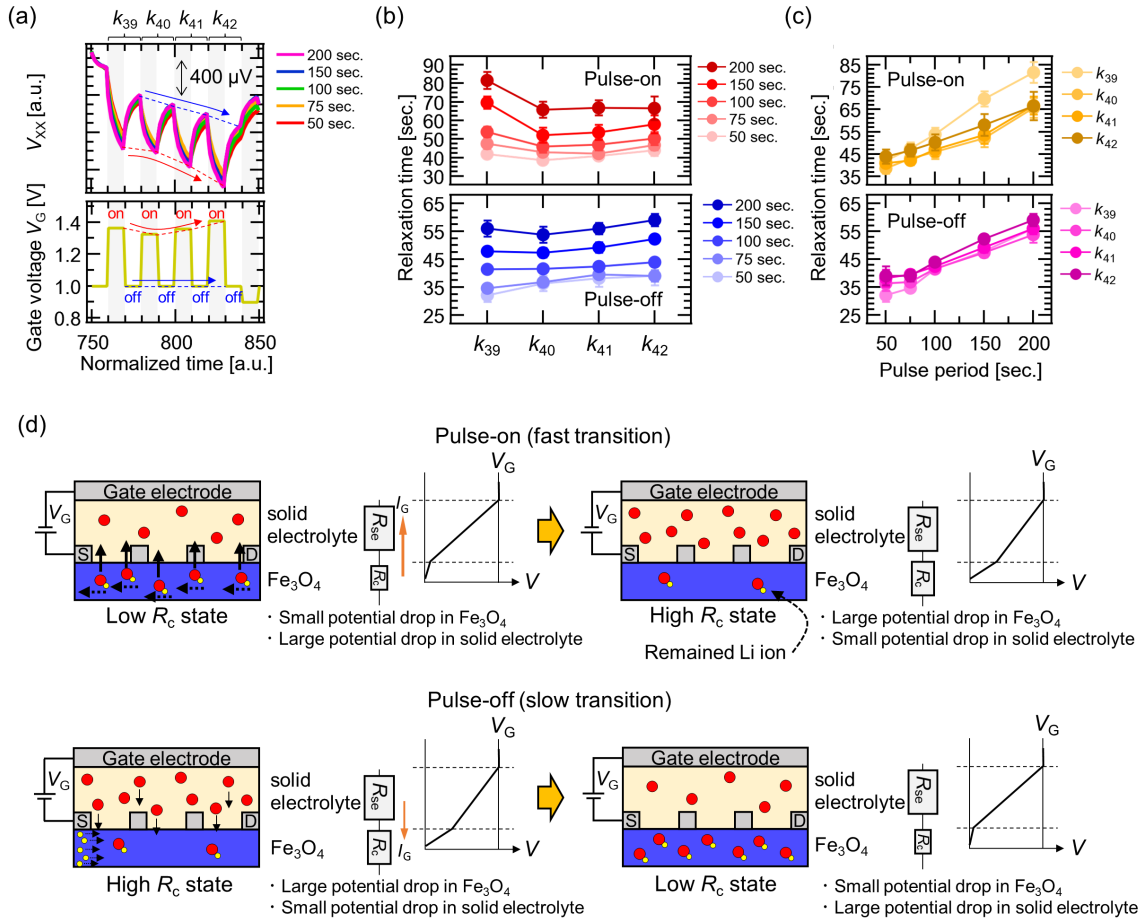
(a)
(b)
(c)
(d)
Normalized time [a.u.]
Pulse period [sec.]
Relaxation time [sec.]
Pulse-on
Pulse-off
200 sec.
150 sec.
100 sec.
75 sec.
50 sec.
400 μV
Gate electrode
solid electrolyte
Fe3O4
Low Rc state
High Rc state
Pulse-on (fast transition)
Pulse-off (slow transition)
Small potential drop in Fe3O4
Large potential drop in solid electrolyte
Remained Li ion

Fig.4